Infill topology optimization of porous structures with discrete variables by the sequential element rejection and admission method

Alain Garaigordobil, Rubén Ansola, Osvaldo M. Querin & Ander Olabarrieta

Taylor & Francis
Taylor & Francis Group

 OPEN ACCESS | Check for updates

Infill topology optimization of porous structures with discrete variables by the sequential element rejection and admission method

Alain Garaigordobil [a], Rubén Ansola [a], Osvaldo M. Querin[b] and Ander Olabarrieta[a]

[a]Department of Mechanical Engineering, University of the Basque Country, Bilbao, Spain; [b]Department of Mechanical Engineering, University of Leeds, Leeds, UK

ABSTRACT

This article presents an infill topology optimization procedure to generate lightweight porous structures. The proposed method is based on discrete variables and builds upon the sequential element rejection and admission method, extending previous work on topology optimization for infill structures. Local volume constraints are introduced in the conventional formulation of the topology optimization problem for maximum stiffness design instead of the global volume constraint. The local constraints are applied, dividing the interior of a given design shape into quadrangular subdomains with variable aspect ratios. The localized material within these subordinate cells is allowed to flow between two discrete material models, 'real' and 'virtual', where two separate criteria are considered for the rejection and admission of elements. The results demonstrate the effectiveness of the method, showing that detailed porous designs are efficiently achieved with the proposed strategy. Numerical examples demonstrate the effects of the different design parameters.

1. Introduction

Topology optimization has been extensively studied over the past few decades, and it can now be considered a mature structural design method. This optimization strategy has widely penetrated the engineering community, particularly in the aerospace and automotive industries, and designers have benefited from these investigations to find optimized material distributions that maximize the structural performance under given boundary conditions and constraints. Comprehensive summaries on topology optimization can be found in Bendsøe and Sigmund (2004) and in dedicated review articles (Rozvany 2009; Sigmund and Maute 2013; Deaton and Grandhi 2014). The increased availability of additive manufacturing processes and materials has provided new possibilities compared to traditional methods, including design freedom and manufacturing of intricate shapes predicted by topology optimization (Gibson, Rosen, and Stucker 2010).

To exploit additive manufacturing capabilities, it is usual to form lightweight structures by introducing lattice substructures with repetitive cell patterns in the interior of the outer shell of the original model as an integrated part of the manufacturing process. Lattice structures represent an essential structural design feature and are frequently used for lightweight designs (Helou and Kara 2018). This practice favours porous designs, reducing the total material volume and improving the performance

---

of structures (Gao *et al.* 2015). Compared to solid structures obtained by conventional topology optimization, coated structures with porous infill show better performance concerning variable loading and local material deficiencies, although compliance values usually increase. Furthermore, compared to their solid counterparts, coated porous structures can achieve higher strength-to-weight ratios (Lu *et al.* 2014) and increased buckling stability (Clausen, Aage, and Sigmund 2016). Their ability to dissipate heat energy and vibrations is also of interest for advanced structural design (Cheng *et al.* 2018). However, the optimum design of these patterns has only been exploited to a minor degree by topology optimization approaches (Plocher and Panesar 2019).

The interior structure of an element printed using additive manufacturing is known as 'infill' and often presents an anisotropic regular structure previously selected by the user (Wu *et al.* 2016). The infill pattern can also be conceived through visual postprocessing of the previously topologically optimized designs, but this procedure does not guarantee the optimality of the infill configuration, thereby wasting the efforts of the numerical topology optimization step. In this context, recent developments include the redesign and optimization of the infill part, which has become of great interest for developing procedures that include infill design directly in the topology optimization subroutines. Most of these developments extend the well-known density-based topology optimization method called solid isotropic material with penalization (SIMP) to address the infill optimum design problem (Bendsøe 1989; Rozvany, Zhou, and Birker 1992). One of the referring methods (Wu *et al.* 2018) proposed introducing a grouped set of local volume constraints to design porous infill structures within a fixed domain. In other approaches, the optimization of both the exterior shell and the interior infill is considered. A novel method was presented by Clausen, Aage, and Sigmund (2015) to design coated structures where the base material was interpreted as a uniform fill, and the base structure and the coating were separated by introducing a two-step projection strategy. This approach was extended by Wu, Clausen, and Sigmund (2017), who moved a step further and presented a combined solution by concurrently evolving the shell contour and the infill microstructure. Alternative two-scale concurrent topology optimization formulations have also been proposed (Zhang, Wang, and Kang 2019; Kang and Wang 2011), where the local porosity ratio and the global volume ratio are controlled.

Homogenization-based topology optimization has also been examined (Groen, Wu, and Sigmund 2019) for coated structure design with orthotropic infill material. Here, the conventional square unit-cell with a rectangular hole (Bendsøe and Kikuchi 1988) was used to describe the periodic infill, and the projected microstructure was aligned with the directions of lamination. The level-set method has also been used to design the infill region within a previously optimized external contour (Wang and Kang 2018; Dapogny *et al.* 2019). Other emerging topics for topologically optimized and variable-density lattices are multi-scale and multi-material structures, where two different materials are distributed in a combined optimization of macro-scale and micro-scale lattices (Long, Han, and Gu 2017; Da *et al.* 2017).

This article aims to extend the sequential element rejection and admission (SERA) method (Rozvany and Querin 2002) to the field of infill optimization. The authors' preliminary and rough first approximation can be found in Garaigordobil *et al.* (2020), but that content is widely extended and further developed in this article. The control of the porosity level of the structures is studied, including an investigation of the impact of different subdomain sizes and material volume fractions. The influence of subdomain aspect ratios that differ from the conventional 1×1 ratio is also analysed, which permits the development of a novel anisotropic filter that avoids unidirectional material growth. This article also extends to the study and use of multiple subdomain ratios in the same optimization problem.

In summary, the specific contributions of the present article include a topology optimization procedure for porous structures based on the discrete SERA method and an adapted local element rejection and admission process. The procedure can simultaneously work with subdomains of different size and aspect ratios, and features an alternative anisotropic filter that prevents the unidirectional growth of solid members provoked by uniaxial stress regions.

2. Local volume constraint

Two main features characterize porous structures: first, they are composed of intertwined and connected substructures, and secondly, the material is very evenly distributed within the given design domain, as can be seen in Figure 1. The conventional topology optimization problem with a global volume constraint does not lead to structures of this type since material layouts generally describe thick solid regions and large voids. A simple strategy to form porous patterns with topology optimization is to replace the conventional global volume constraint with a set of local volume constraints that control the presence of solid material in small neighbourhoods N_e, as given in Equation (1):

$$g_{Ne} = \frac{V_{Ne}}{V_{Ne\,Tot}} - VF_{Ne}^{Lim} = \frac{\sum_{e \in Ne} \rho_e}{\sum_{e \in Ne} 1} - VF_{Ne}^{Lim} \leq 0 \tag{1}$$

where V_{Ne} and $V_{Ne\,Tot}$ are the material volume and the total volume in the neighbourhood Ne, respectively, and ρ_e is the density of the element e inside Ne. The term VF_{Ne}^{Lim} refers to the upper bound of the volume fraction in the neighbourhood Ne.

Together with the SIMP material interpolation model, the latter constraint was successfully applied to overlapping neighbourhoods (Wu *et al.* 2018). The article resorted to a consolidated high-degree p-norm and aggregated all these constraints into one to prevent the high computational cost that such a strategy would require. In the SERA method, the update rule of the design variables is performed by an evolutionary method, making it manageable to enforce a volume constraint to each subdomain.

In the present work, the original domain Ω, which is discretized with unit square finite elements, is split into a finite number of non-overlapping rectangular subdomains Ω_S of size $R_1^s \times R_2^s$ (Figure 2). The volume fraction is constrained in these smaller regions, favouring the formation of substructures and driving the optimization problem towards a more even material distribution.

The local constraint that restricts the presence of material volume in a subdomain is given in Equations (2) and (3):

$$g_s = VF_s - VF_s^{Lim} \leq 0 \qquad / \qquad s = 1, \ldots, S \tag{2}$$

$$VF_s = \frac{V_s}{V_{s\,Tot}} = \frac{\sum_{e \in s} \rho_e}{R_1^s \cdot R_2^s} \qquad / \qquad s = 1, \ldots, S \tag{3}$$

The term VF_s is the volume fraction of the sth subdomain, computed as the ratio of its material volume V_s to its total volume $V_{s\,Tot}$. VF_s^{Lim} is the upper bound volume fraction for the sth subdomain, and S is the total number of subdomains. The size and aspect ratio can be similar for all subdomains,
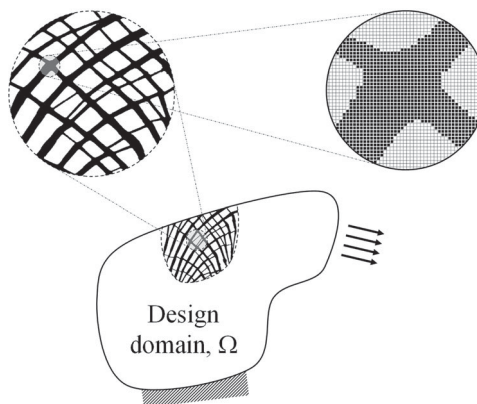

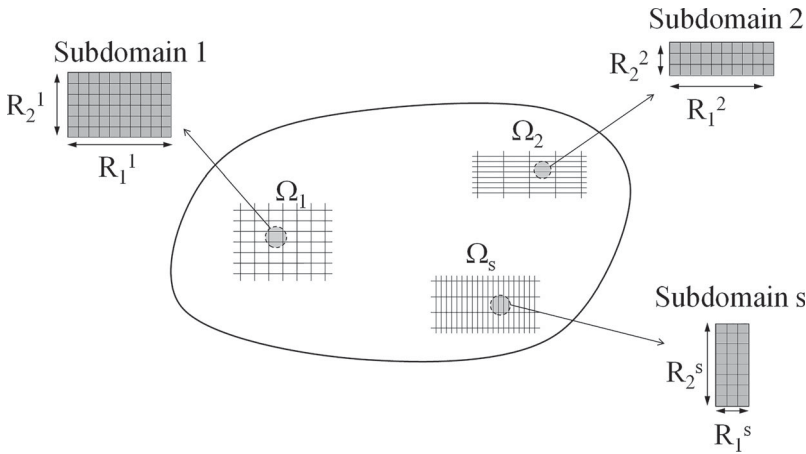**Figure 1.** Infill design of a porous structure.

Figure 2. Division of the design region into subdomains.

although subdomains of different sizes can be used to (1) deal with highly anisotropic stress fields, (2) avoid poorly connected regions, and (3) avoid weak regions.

Note that the inequality constraint given in Equation (2) explicitly implies that the sth subdomain must retain a material volume fraction no greater than the local volume fraction upper bound. Then, the set of local volume constraints implicitly imposes an upper bound on the total volume, *i.e.* if all local material volume upper bounds are equal to the desired global counterpart, $VF_s^{Lim} = VF^{Lim}$ for all s; the global constraint is implicitly included in the problem, which eliminates the necessity of adding it to the formulation.

3. Problem formulation

In this work, the problem of determining the optimum design of porous structures is formulated as a maximum stiffness problem. The objective is to find the material distribution that minimizes the structure's compliance under prescribed support and loading conditions. This formulation is based on a finite element discretization of the design domain Ω, as in Equations (4)–(7):

$$\text{Minimize:} \quad c(\boldsymbol{\rho}) = \boldsymbol{U}^T \cdot \boldsymbol{K} \cdot \boldsymbol{U} \tag{4}$$
$$\boldsymbol{\rho}$$

$$\text{Subject to :} \quad \boldsymbol{K} \cdot \boldsymbol{U} = \boldsymbol{F} \tag{5}$$

$$g_s(\boldsymbol{\rho}) \leq 0 \quad / \quad s = 1, \ldots, S \tag{6}$$

$$\rho_e = \{\rho_{min}, 1\} \tag{7}$$

where $c(\boldsymbol{\rho})$ is the structure's compliance, $\boldsymbol{\rho}$ is the vector of design variables (elemental densities), $\boldsymbol{U}$ and $\boldsymbol{K}$ are the displacement vector and the global stiffness matrix, respectively, and $\boldsymbol{F}$ is the applied load vector. The set of local volume constraints in Equation (6) prevents the formation of thick solid regions and large voids. In addition, as in conventional topology optimization problems, the algorithm is expected to use the maximum allowable material volume in each subdomain. Finally, the parameter ρ_{min} is the minimum elemental density, given a value of 10^{-9}. Since SERA is a discrete method, the elemental density values (ρ_e) are either ρ_{min} or 1, representing void (virtual) or solid (real) material, respectively.

4. Material rejection and admission process for infill optimization

Section 2 introduced the subdomain level material volume evaluation, and such computations ultimately proceed to a local procedure for rejecting and admitting the material. The following subsections describe the conventional SERA and how the optimization process in Ansola Loyola *et al.* (2018) is adapted to the infill optimization to form porous structures.

4.1. Conventional SERA optimization process

The SERA method is a bidirectional evolutionary method and works with two separate criteria for adding and removing material from the design domain. Solid or 'real' material is removed (turned void) while void or 'virtual' material is added (turned solid). The conventional procedure that generally starts from a fully filled domain simultaneously classifies the finite elements into two lists, one for all of the solid material and one for all of the void material. The two lists are ordered in an ascendant way according to the element sensitivity number or driving criterion number (Cv). The latter is the main novelty of the SERA method compared to other evolutionary methods such as bidirectional evolutionary structural optimization (BESO) (Querin, Steven, and Xie 1998), which do not differentiate between the sensitivities of solid and void material.

In the conventional method, the material rejection and admission process is a two-stage process. First, different amounts of material are added and removed in each iteration until the target volume fraction VF^{Lim} is reached. The second stage starts when the objective volume fraction is met, and the material is redistributed by adding and removing the same amount until the problem converges.

During the first stage of the optimization problem, the iteration-wise target volume fraction $VF(i)$ is calculated using Equation (8). This value sets the volume fraction that must be reached in the following iteration of the optimization problem. The total fraction of material volume to be removed in the ith iteration is given by Equation (9). The latter amount is separated into the volume fraction to be added, $\Delta V_{Add}(i)$, and the volume fraction to be removed $\Delta V_{Rem}(i)$, using Equations (10) and (11), respectively (Figure 3a, b). As seen in Figure 3, the iteration-wise material rejection and admission process consists of two substeps. For a full initial design domain, to decrease the global volume fraction, more material is removed than is added during the first stage of the optimization process. On the other hand, the second stage adds and removes the same amount of material, so that the volume of material remains constant (Equation 12).

$$VF(i) = \max((VF(i-1) \cdot (1 - PR)), V^{Lim}) \tag{8}$$

$$\Delta V(i) = |VF(i) - VF(i-1)| \tag{9}$$

$$\Delta V_{Add}(i) = \Delta V(i) \cdot (SR - 1) \tag{10}$$

$$\Delta V_{Rem}(i) = \Delta V(i) \cdot SR \tag{11}$$

$$\Delta V_{Add}(i) = \Delta V_{Rem}(i) = \beta \cdot V^{Lim} \tag{12}$$

Finally, the procedure used by the algorithm to reject and add elements is performed according to their elemental driving criterion value (Cv_e) relative to two global threshold driving criterion values, Cv_R^{thr} and Cv_V^{thr}, respectively (Figure 3c).

The three parameters governing the problem are described as follows:

- The progression rate (PR) controls how SERA removes material from and introduces material into the design domain.
- The smoothing ratio (SR) controls the net level of excess material to be either introduced into or removed from the design domain.
- The material redistribution fraction (β), used only when the target volume is reached, controls the small constant amount of material that is redistributed until the criterion distribution converges.
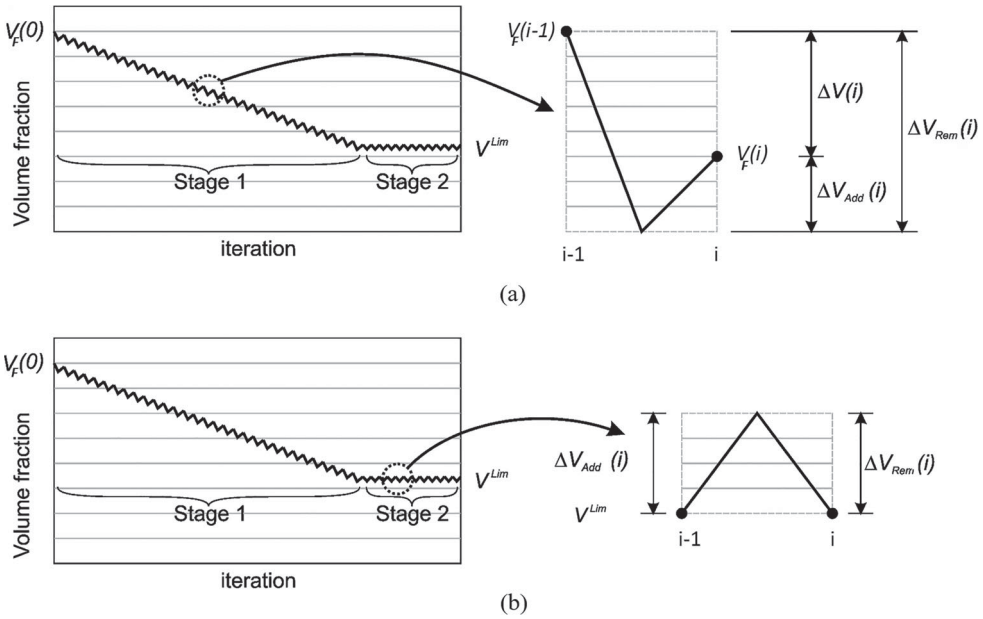
Figure 3. Material rejection and admission process: (a) first stage of the process; (b) second stage of the process; (c) material status updating process.

In the optimization of structures, typical ranges for values of these parameters are: $0.01 \leq PR \leq 0.09$, $1.2 \leq SR \leq 1.9$ and $0.001 \leq \beta \leq 0.005$.

In infill optimization, the local optimization of the subdomains requires a modification of the above summarized global procedure. In fact, in the adapted version, the iteration-wise number of elements to be rearranged is defined at the subdomain level, and the material rejection and admission process is performed locally.

4.2. Determination of the local volume fraction to be rearranged

Note that Equations (8)–(12) perform global volume computations, and the volume fractions given by Equations (10)–(12) refer to the material volume fractions that must be both rejected from and added to the whole design domain. To obtain porous designs, the process described in Figure 3 must be performed locally at the subdomain level. The necessary changes to adapt the conventional process to infill design optimization are introduced in the following.

First, to operate at the subdomain level, it becomes essential to know how much material needs to be rearranged in each subdomain and the number of elements to add and remove. One straightforward way of determining the local volume fractions to be added and removed is to distribute $\Delta V_{Add}(i)$ and $\Delta V_{Rem}(i)$ along the different subdomains. In that case, each subdomain will add a proportion of material $\Delta V_{Add}(i)$ and remove a proportion of material $\Delta V_{Rem}(i)$, distributing the material volume variation among all the subdomains. This strategy is demonstrated in Equations (13)–(15) to maintain compliance with the volume fraction:

$$\Delta V(i) \cdot V_{Tot} = \Delta V(i) \cdot \sum_{s \in \Omega} V_{sTot} = \Delta V(i) \cdot V_{1Tot} + \ldots + \Delta V(i) \cdot V_{STot} \tag{13}$$

$$\Delta V_{Add}(i) \cdot V_{Tot} = \Delta V_{Add}(i) \cdot \sum_{s \in \Omega} V_{sTot} = \Delta V_{Add}(i) \cdot V_{1Tot} + \ldots + \Delta V_{Add}(i) \cdot V_{STot} \tag{14}$$

$$\Delta V_{Rem}(i) \cdot V_{Tot} = \Delta V_{Rem}(i) \cdot \sum_{s \in \Omega} V_{s \, Tot} = \Delta V_{Rem}(i) \cdot V_{1 \, Tot} + \ldots + \Delta V_{Rem}(i) \cdot V_{S \, Tot} \qquad (15)$$

where V_{Tot} is the total volume of the design domain, and $V_{s \, Tot}$ is the total volume of the sth subdomain.

Once the volume fractions to be added and removed are known for each subdomain, the number of elements to which they correspond can be calculated by Equations (16) and (17). Since the presented formulation allows subdomains of unlike sizes and aspect ratios, the different subdomains can trade with different amounts of elements.

$$\Delta E_{Rem}^s(i) = \Delta V_{Rem}(i) \cdot R_1^s \cdot R_2^s \qquad (16)$$

$$\Delta E_{Add}^s(i) = \Delta V_{Add}(i) \cdot R_1^s \cdot R_2^s \qquad (17)$$

4.3. Local material rejection and admission process

As introduced in Section 4.1, the conventional procedure considers the global sensitivity matrix to perform the material rejection and admission process, and rejects and adds elements according to their elemental driving criterion value (Cv_e) relative to two global threshold driving criterion values, Cv_R^{thr} and Cv_V^{thr}, respectively. On the other hand, the adapted procedure considers only the driving criterion values of the elements within the same subdomain. A pair of sensitivity lists per subdomain contains the sensitivity values of $R_1^s \cdot R_2^s$ elements ordered in an ascendant way, and a local material rejection and admission process is performed for each pair (Figure 4).

Since the optimization problem is defined as the minimization of the compliance of the design domain, the switching elements are those located at the bottom of the lists; therefore, the solid elements with a driving criterion value below Cv_{ThR}^s turn void, and void elements below Cv_{ThV}^s turn solid.

The local threshold driving criterion values for solid ($Cv_{Th_R^s}$) and void ($Cv_{Th_V^s}$) elements are calculated using Equations (18) and (19), and they respond to the $\Delta E_{Rem}^s(i)$th and $\Delta E_{Add}^s(i)$th elements
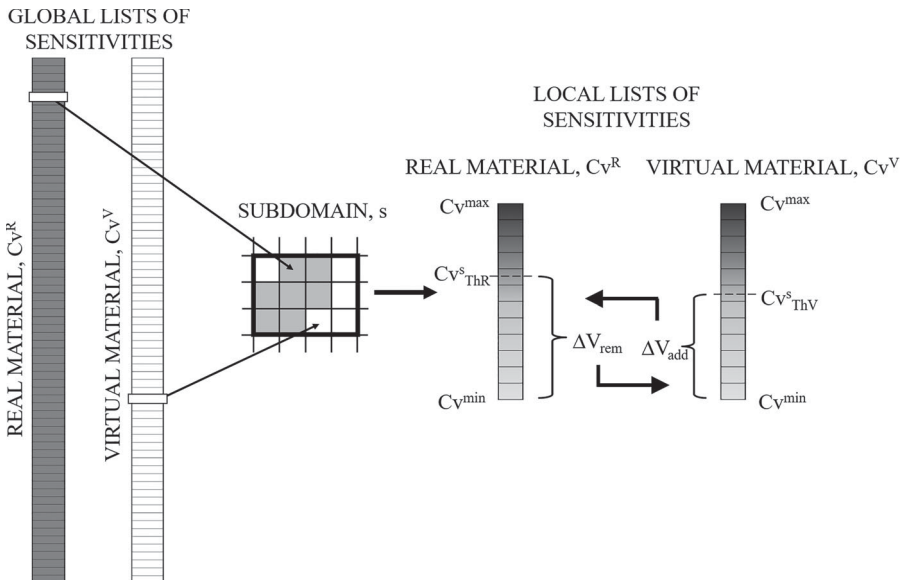

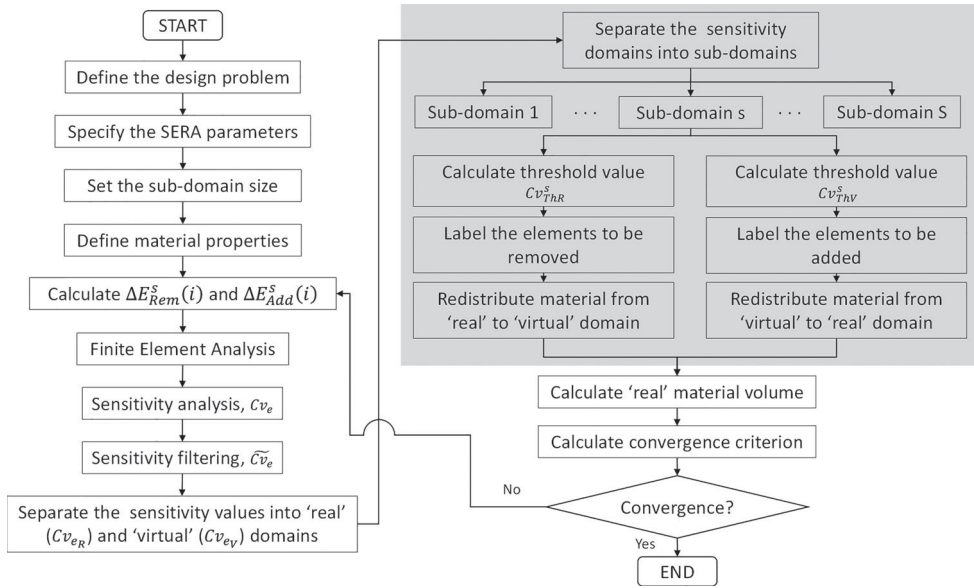**Figure 4.** Local material rejection and admission process.

Figure 5. Flowchart for infill optimization. SERA = sequential element rejection and admission.

at the bottom of the corresponding list.

$$Cv_{Th_R^s} = Cv_{e_R}(R_1^s \cdot R_2^s - \Delta E_{Rem}^s(i), 1) \tag{18}$$

$$Cv_{Th_V^s} = Cv_{e_V}(R_1^s \cdot R_2^s - \Delta E_{Add}^s(i), 1) \tag{19}$$

A quick overview of the whole optimization process is provided in the flowchart of Figure 5, where the operations concerning local subdomains are highlighted separately.

5. Sensitivity analysis

After the finite element analysis, a sensitivity analysis is carried out to determine how sensitive the objective function is to adding or removing the elements. The sensitivity or driving criterion (Cv_e) computation process of the SERA is not included in this work, but the reader can find extensive explanations in Ansola Loyola *et al.* (2018) and Querin *et al.* (2017). The expressions of the elemental driving criterion for solid or real material (Cv_{e_R}) and void or virtual material (Cv_{e_V}) are given by the following equations:

$$Cv_{e_R} = \alpha_{e_R} = \boldsymbol{U}_e^T \cdot \boldsymbol{k}_e \cdot \boldsymbol{U}_e \tag{20}$$

$$Cv_{e_V} = \alpha_{e_V} = -\boldsymbol{U}_e^T \cdot \boldsymbol{k}_e \cdot \boldsymbol{U}_e \tag{21}$$

where $\boldsymbol{U}_e$ is the displacement vector of element e due to the applied loads and $\boldsymbol{k}_e$ represents the elemental stiffness matrix.

6. Filtering of sensitivities

To avoid any instability and chequerboard problems, a sensitivity filtering step is included in the formulation, which is globally performed over the whole design domain. Performing global filtering ensures that the sensitivity values of the elements in adjacent subdomain borders are similar, which has been proven effective to guarantee the continuity of substructures in contiguous subdomains.

The proposed procedure introduces a single filtering step and, since SERA is a discrete method, no additional projection techniques are required to make the density field binary. The mesh-independent filter is based on the technique proposed by Sigmund and Petersson (1998) and modifies each element's sensitivity number based on a weighted average of the element sensitivities in a fixed neighbourhood defined by a minimum radius r_{min} (Equation 22).

$$\tilde{\alpha}_e = \frac{\sum_{j=1}^{N} w_j \cdot \rho_j \cdot \alpha_j}{\rho_e \cdot \sum_{j=1}^{N} w_j} \tag{22}$$

$$w_j = \max(0, r_{min} - dist(e, j)) \tag{23}$$

where $\tilde{\alpha}_e$ is the filtered sensitivity number of the eth element, N is the number of elements in the domain, and ρ_j and α_j are, respectively, the density and the sensitivity number of the jth element. According to Equation (23), the weighting factor w_j for element j decreases linearly the further the element j is from the element e, where $dist(e, j)$ is the distance between the centres of the two elements. For all elements outside the filter radius, the weighting factor is equal to zero.

7. Convergence criterion

The convergence criterion evaluates the change in the objective function in the last 10 iterations and is given by Equation (24). This number of iterations was found to be adequate for convergence to take place. This implies that the process will have a minimum of 10 iterations, as the convergence is not applied until the 10th iteration.

$$\varepsilon_i = \frac{\left| \sum_{i-9}^{i-5} c_i - \sum_{i-4}^{i} c_i \right|}{\sum_{i-4}^{i} c_i} < \varepsilon_{Lim} \tag{24}$$

where i is the current iteration number (greater than 10), c_i is the objective function value from Equation (4) in the ith iteration, ϵ_i is the convergence value of the objective function in the ith iteration, and ϵ_{Lim} is the convergence limit, which controls when to terminate the optimization process.

8. Examples

This section presents four examples to demonstrate the effectiveness of the procedure for generating optimum infill designs. These are: (1) a cantilever beam, (2) the Messerschmitt–Bölkow–Blohm (MBB) beam, (3) an axially loaded beam, and (4) an L-shaped beam. Each example studies a specific parameter of the optimization problem or introduces a new capacity of the proposed approach. The cantilever beam is used to show the effect of varying the volume fraction and filtering radius on the connectivity of the infill topology. The MBB beam example shows the effect of varying the subdomain size on the emerging infill topology. Then, anisotropic stress fields are studied through an axially loaded (traction) beam, and a strategy to deal with them is proposed, changing the aspect ratio of the subdomains according to the orientation of the dominating principal stress. Finally, an L-beam is presented to introduce the possibility of simultaneously working with multiple subdomain sizes and aspect ratios inside the same domain. In the examples, Young's modulus of the solid material is 1 and 10^{-9} for the void, and Poisson's ratio is 0.3.

8.1. Cantilever beam

This example tests the classical two-dimensional cantilever beam with the geometry and loading conditions described in Figure 6(a). The beam is discretized with 1200×600 square unit finite elements,
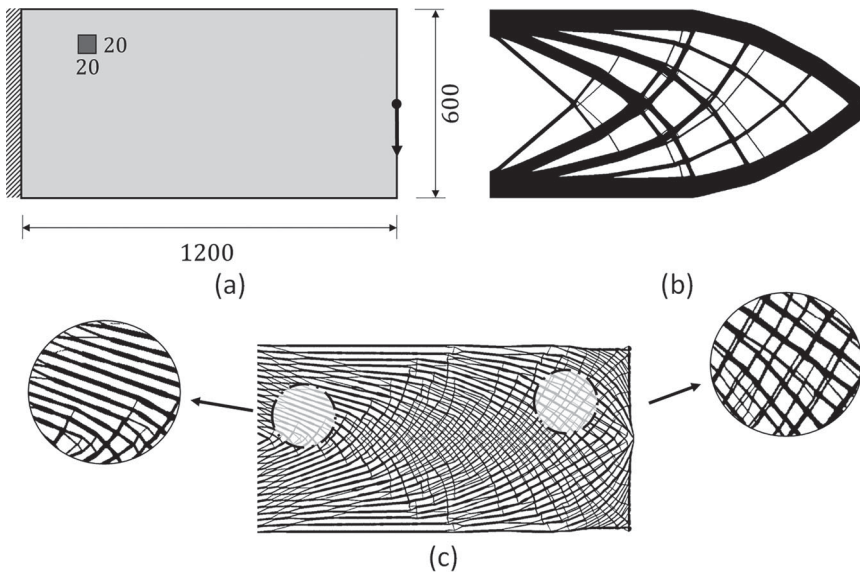
Figure 6. (a) Design domain for the cantilever beam; (b) conventional cantilever beam after topology optimization, $c = 146.0773$; (c) optimized porous design for $R_1 \times R_2 = 20 \times 20$ subdomains, $c = 229.289$.

a downward vertical unit force is applied on the middle point of the right edge, and all degrees of freedom are restricted in the left edge. The objective volume fraction is set to $V^{Lim} = 0.4$ and the filter radius is set to $r_{min} = 2$.

The regular topology optimization result of the cantilever beam given in Figure 6(b) shows how, without the set of local volume constraints, SERA deposits solid material forming thick members and favours the nucleation of large void areas. When the same optimization problem is performed with the adapted SERA method, which includes the set of local volume constraints in substitution of the global volume fraction constraint, the problem converges into the more intricate material distribution shown in Figure 6(c), a structure formed by intertwined and connected substructures with subdomains of size $R_1 \times R_2 = 20 \times 20$.

Both results show apparent differences in the material layout and, compared to the conventional result, the porous design describes a more uniformly distributed material layout, with tiny pores in place of the former large voids. The local volume constraints compel the subdomains to retain a percentage of solid material deposited along the direction of the principal stresses. In areas with dominant principal stress, this strategy may yield single-directional material layouts, as shown in the details of Figure 6(c). The compliance values of these designs, given in the caption to Figure 6, are very unalike, with the porous design being the most compliant. The decay of the stiffness is due to retention of the same amount of solid material in every subdomain. The porous design may be more compliant, but it is more robust concerning variations in the load case and enhances the fail-safe behaviour.

Next, the filter radius and the volume fraction are studied to gain a notion of the values that will be used in the rest of the examples. The previously presented design domain is considered again, which is optimized with the same SERA parameters and subdomains of size $R_1 \times R_2 = 20 \times 20$. Figure 7 gathers the results obtained for varying filter radius and volume fractions.

The obtained material distributions resemble porous structures for every combination of filter radius and material volume fraction. The topologies are mainly populated by crossing substructures, except for a few parts at the top and the bottom where elongated substructures are found. Such uni-axial material layout agrees with the stress distribution in these areas, and the algorithm prioritizes the dominant principal stress direction.
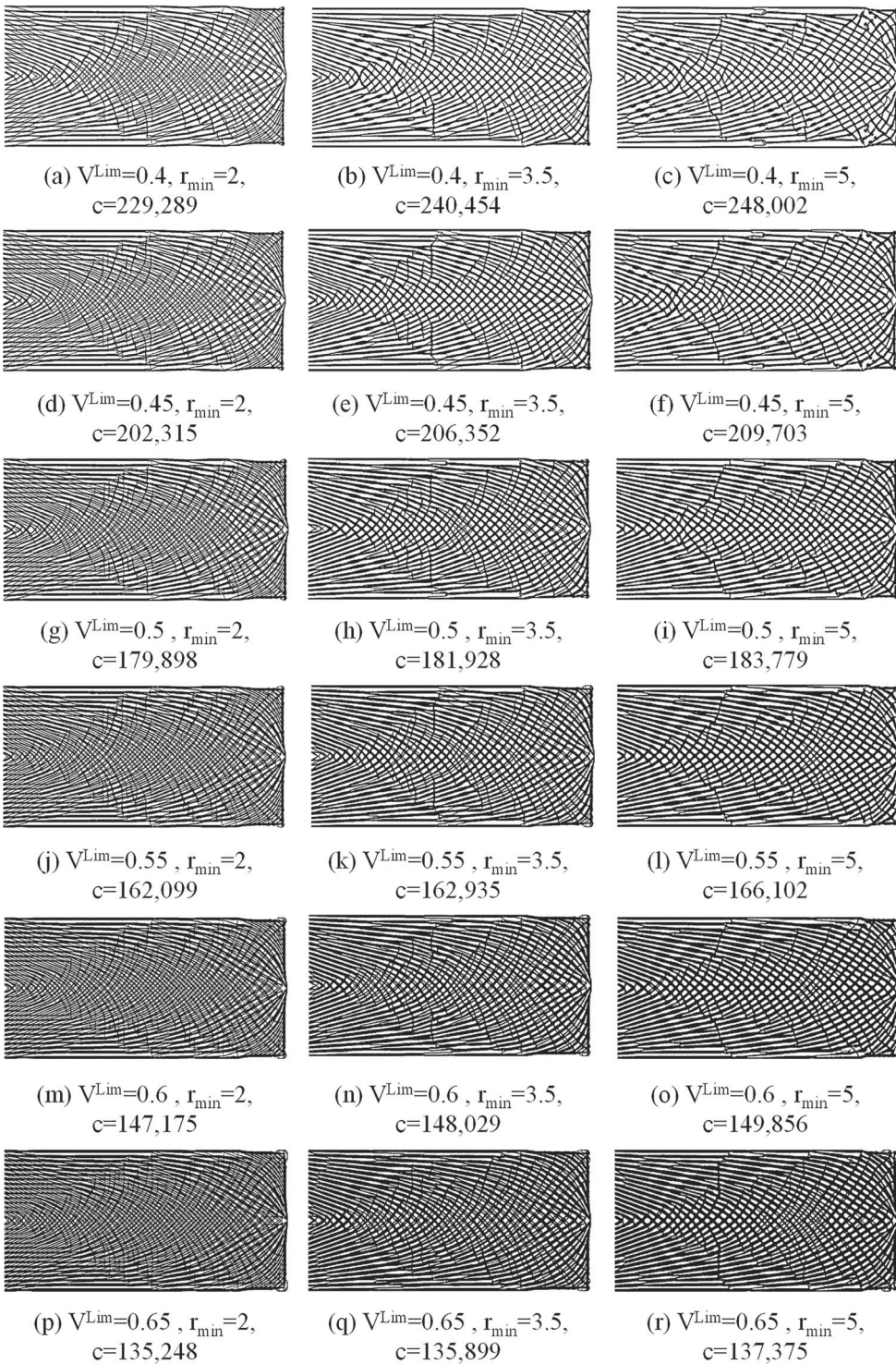
(a) V^{Lim}=0.4, r_{min}=2, c=229,289

(b) V^{Lim}=0.4, r_{min}=3.5, c=240,454

(c) V^{Lim}=0.4, r_{min}=5, c=248,002

(d) V^{Lim}=0.45, r_{min}=2, c=202,315

(e) V^{Lim}=0.45, r_{min}=3.5, c=206,352

(f) V^{Lim}=0.45, r_{min}=5, c=209,703

(g) V^{Lim}=0.5 , r_{min}=2, c=179,898

(h) V^{Lim}=0.5 , r_{min}=3.5, c=181,928

(i) V^{Lim}=0.5 , r_{min}=5, c=183,779

(j) V^{Lim}=0.55 , r_{min}=2, c=162,099

(k) V^{Lim}=0.55 , r_{min}=3.5, c=162,935

(l) V^{Lim}=0.55 , r_{min}=5, c=166,102

(m) V^{Lim}=0.6 , r_{min}=2, c=147,175

(n) V^{Lim}=0.6 , r_{min}=3.5, c=148,029

(o) V^{Lim}=0.6 , r_{min}=5, c=149,856

(p) V^{Lim}=0.65 , r_{min}=2, c=135,248

(q) V^{Lim}=0.65 , r_{min}=3.5, c=135,899

(r) V^{Lim}=0.65 , r_{min}=5, c=137,375

Figure 7. Topologies for the porous design of a cantilever beam with different filter radii and volume constraints.

The results in Figure 7 are accompanied by the corresponding value of the objective function, showing the direct relationship between the filter radius and the structure's compliance. As the filter radius is lowered, the value of the objective function also decreases. It is also noted that large volume fractions counteract the effect of the filter radius, and as the volume fraction approaches the unit value, the compliances converge to a similar value. The filter radius also controls the level of detail and the porosity of the resulting design. Looking at any two results in the same row of Figure 7, *i.e.* two designs with equal volume fraction but different filter radii, it is quickly appreciated that the largest porosity level is obtained with the lower filter radius, and although the general aspect of the two structures is much alike, the level of detail can vary significantly. Therefore, it can be concluded that a small radius favours the formation of thinner substructures and increases the porosity of the structure. Finally, it should be noted that all of the results demonstrate good connectivity between any substructure and the substructures that surround it.

8.2. MBB beam

The second example analyses the optimization case of an MBB beam and studies the use of subdomains of different sizes. Taking advantage of symmetry, the design domain (Figure 8a) is discretized using a fine mesh of 1200×600 unit square finite elements. A vertical unit force is applied in the left upper node, and the horizontal and vertical displacements are restricted in the nodes in the left-hand edge and the right lower node, respectively. The objective volume fraction is set to $V^{Lim} = 0.4$ and, to achieve an intermediate porosity level, the filter radius is set to $r_{min} = 3$. For the infill design in Figure 8(b), the subdomains are of size $R_1 \times R_2 = 30 \times 30$ elements.

The proposed infill optimization procedure allows the definition of subdomains of different sizes, which implicitly gives the designer the ability to control the porosity level of the final material layout. Theoretically, the subdomains can be as small as the unit element or as big as the design domain itself. In the following, different subdomain sizes ranging from $R_1 \times R_2 = 20 \times 20$ to 600×600 are analysed, plus one additional case where a unique subdomain covers the whole domain. Their relative sizes are shown in Figure 9, and the obtained optimized topologies are gathered in Figure 10.

It can be seen that smaller subdomain sizes lead to greater porosity levels, and the resulting material distribution moves closer to the conventional result as they become larger. Therefore, the structure becomes stiffer but loses the benefits of porous structures. When the shape and size of the subdomain match the geometry of the whole design domain, the conventional topology optimization result emerges. It can be said that the stiffness of the porous structure is strongly related to the size of the subdomains, as demonstrated in the following text.

When the size is neither small enough to form highly porous structures nor large enough to approach the classical topology optimization result, a certain amount of leftover material appears in the upper right corner of the structure. This material lies within a single subdomain and corresponds
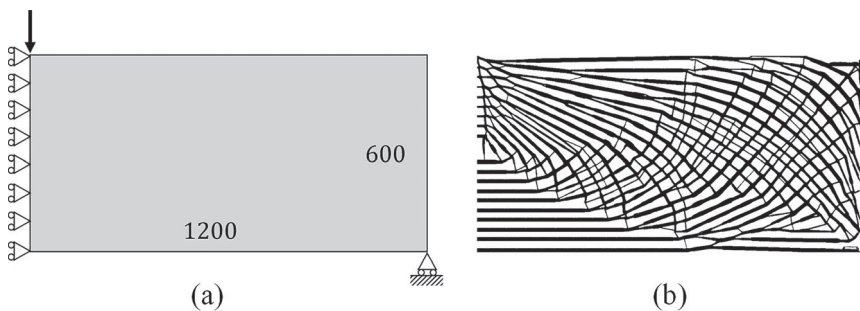

Figure 8. (a) Design domain of a Messerschmitt–Bölkow–Blohm (MBB) beam; (b) optimized porous design. $R_1 \times R_2 = 30 \times 30$, $c = 145.488$.
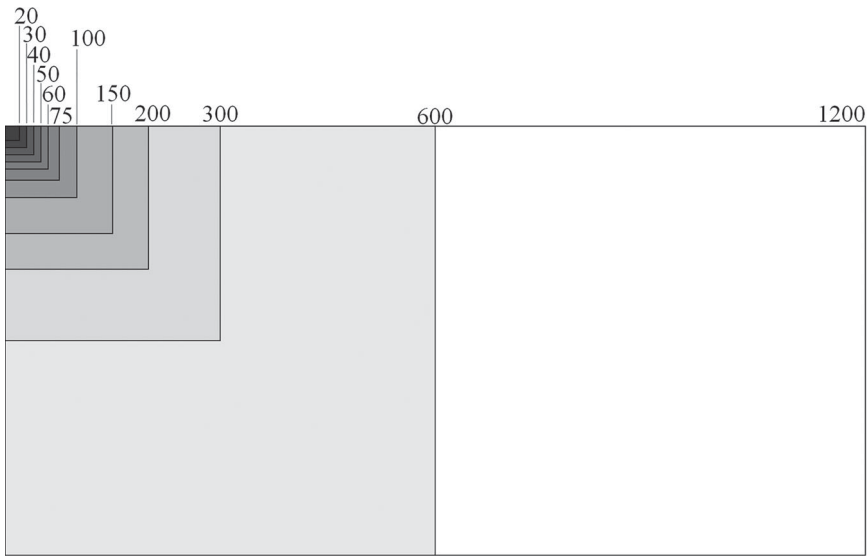
Figure 9. Relative sizes of the subdomains.

(a) R1 = R2 = 20

(b) R1 = R2 = 30

(c) R1 = R2 = 40

(d) R1 = R2 = 50

(e) R1 = R2 = 60

(f) R1 = R2 = 75

(g) R1 = R2 = 100

(h) R1 = R2 = 150

(i) R1 = R2 = 200

(j) R1 = R2 = 300
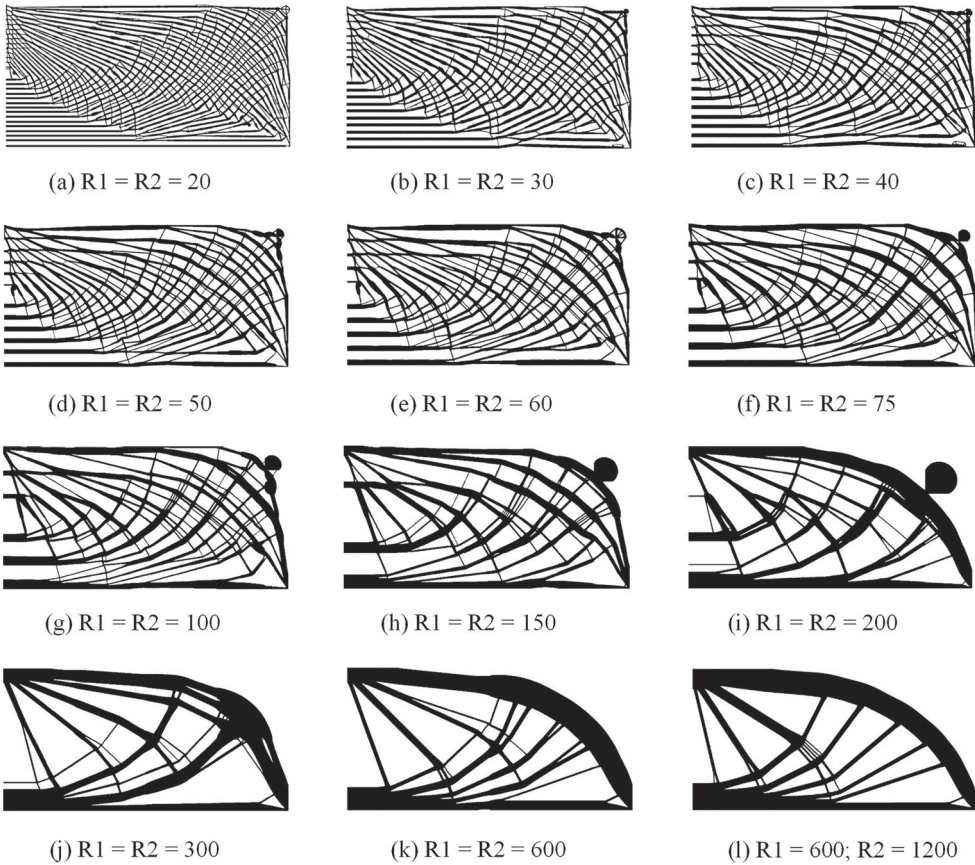
(k) R1 = R2 = 600

(l) R1 = 600; R2 = 1200

Figure 10. Results obtained for varying subdomains sizes.

to the prescribed fraction of the total available volume inside that cell. The leftover material emerges because the algorithm forces the presence of an amount of material in every cell. Therefore, some particular subdomain sizes may lead to this sort of material supplement being inefficiently attached to the structure's body.

The obtained results also demonstrate that the proposed procedure guarantees the connectivity of the substructures formed within the different subdomains. No discontinuity is appreciable, either when the subdomains are small or when they have a considerable size. That is to say, independently of the subdomain size, the substructure formed within a subdomain is smoothly connected with the adjacent material.

8.3. Axially loaded beam: anisotropic filter

The third example is the optimization case of the axially loaded beam, an exercise that requires a procedure to deal with uniaxial material distributions due to anisotropic stress fields. Figure 11(a) shows the design domain that is discretized with a fine mesh of 1200×600 unit square elements. The left edge of the beam is fixed, and a horizontal and distributed force is applied on the right side nodes with unit value. In the optimized results, the objective volume fraction is set to $V^{Lim} = 0.6$ and the size of the subdomains is $R_1 \times R_2 = 30 \times 30$ elements. Some of the obtained results possessed many pores; therefore, to control the porosity level and favour the visualization of the results, the filter radius is set to $r_{min} = 5$ elements.

Once again, the regular topology optimization result (Figure 11b) shows how SERA deposits solid material forming thick regions, while the adapted procedure leads the problem to the material distribution shown in Figure 11(c). Nevertheless, the latter is solely composed of horizontal bars that connect the load points with the clamp. It is a reasonable solution considering that the subdomains are compelled to retain a certain amount of material, but it hardly complies with the description of a porous structure. For instance, no interconnected substructures can be seen, and the structure is weak to any vertical variation in the load. This issue is due to this particular case's highly anisotropic stress field, where the dominant principal direction is horizontal. Although the structures in Figure 11(b) and (c) provide great stiffness, the aim is to achieve a porous design; therefore, to avoid great areas with unidirectional growth, an anisotropic filtering technique is introduced.
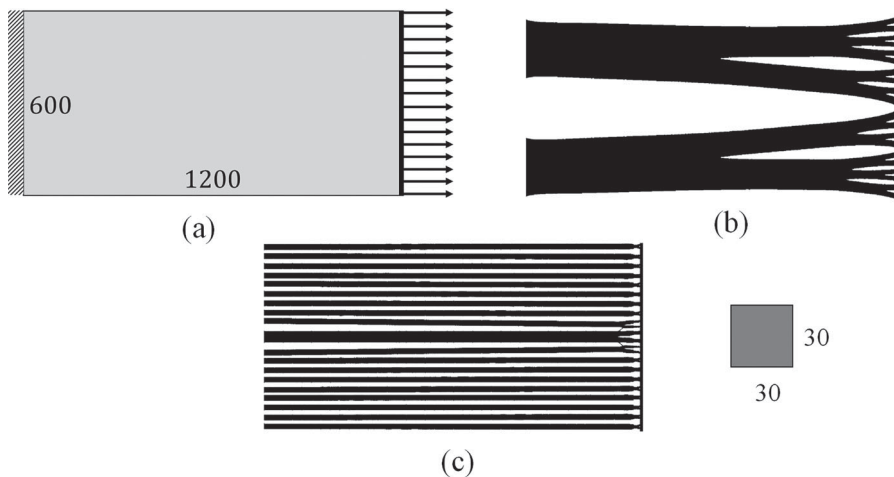

Figure 11. (a) Design domain of the axially loaded beam; (b) conventional topology optimization result, $c = 307,669.642$; (c) optimization with local volume constraints. $R_1 \times R_2 = 30 \times 30$, $c = 612,503.935$).
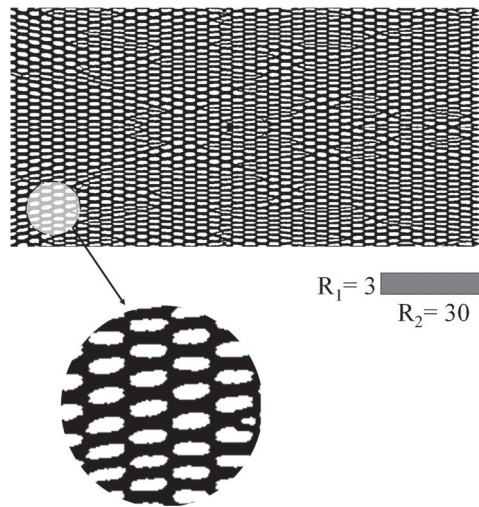
Figure 12. Porous design of an axially loaded beam. $c = 790,776.255$.

The design domain in Figure 11(a) is considered one more time. The values of all optimization parameters are preserved except for the subdomain size, which is set to $R_1 \times R_2 = 3 \times 30$ elements. The largest side of the subdomains is parallel to the dominant principal direction. With this simple modification, the problem converges to the material layout shown in Figure 12.

As can be seen, the resulting topology is highly porous, with, in this case, substructures of gyroid shapes, demonstrating that the proposed anisotropic filter avoids unidirectional growth and favours obtaining results closer to trabecular structures. This new design should provide all of the qualities and improved robustness of a porous structure compared to the previous design in Figure 11(c). An example is provided to demonstrate how the avoidance of the elongated substructures can improve this feature.

Two previously optimized tensile beams are studied under the influence of a variation in their load direction. A variation of 45° is considered, resulting in a distributed inclined load with unit value in each node of the right side contour. The displaced configurations of the two designs are shown in Figure 13, where it is seen that the porous design has better tolerance to the proposed variation in the load direction. Proof of this is that the general compliance decays by 68.82% with respect to the non-porous design.
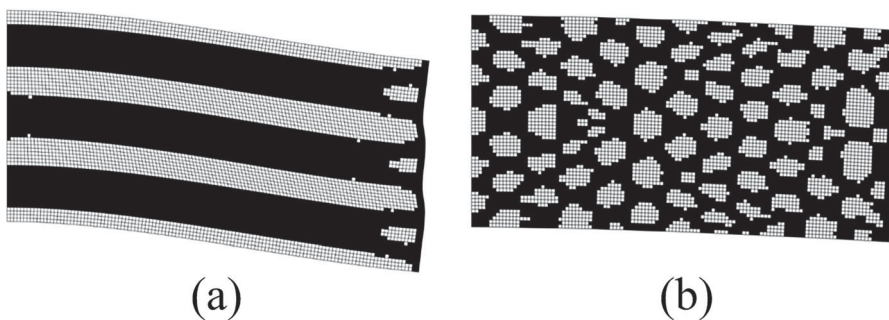

(a)   (b)

Figure 13. Deformation under a leaned distributed load with 45° inclination of two optimized tensile beams: (a) design with elongated substructures, $c = 848,760$; (b) porous design, $c = 264,600$.

8.4. L-beam: multiple subdomain sizes

The final example is the optimization case of an L-beam, the design domain of which is shown in Figure 14(a). The domain is discretized with 900×900 unit square finite elements, a vertical force is applied in the right upper node and the structure is clamped on the upper left side. A first optimization is performed with the conventional algorithm, with $V^{Lim} = 0.6$ and $r_{min} = 5$. The optimization process converges to the topology given in Figure 14(b). This topology is composed of two differentiable regions, a vertical part that is subjected to combined axial and bending with an absent shear effort, and a horizontal part subjected to simple bending. The combination of axial and bending efforts in the vertical part makes it susceptible to uniaxial material growth, as proven in Figure 15(a) with the porous design obtained for square subdomains of size $R_1 \times R_2 = 30 \times 30$.

    To avoid the elongated substructures seen in Figure 15(a), the anisotropic filter proposed in Section 8.3 is applied, which yields the material distribution shown in Figure 15(b). As can be seen, the stretched subdomains promote the formation of multidirectional substructures in the vertical part
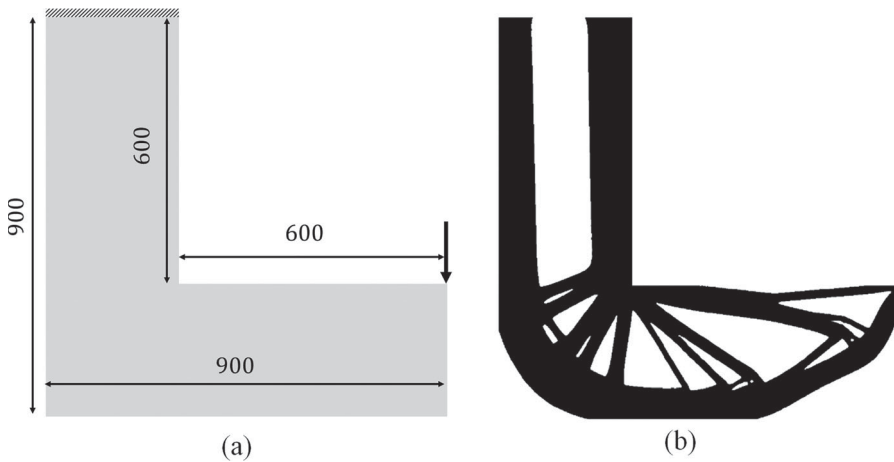

Figure 14. (a) Design domain of the L-beam; (b) topology optimization result, $c = 298.093$.
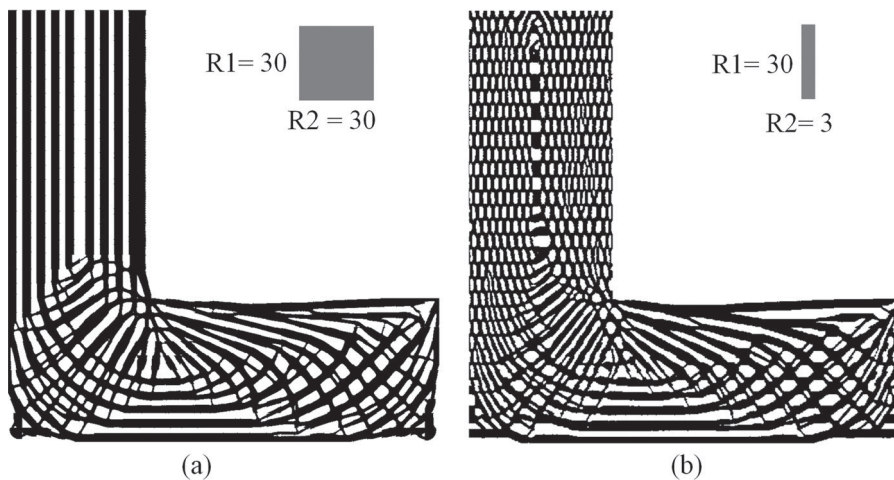

Figure 15. (a) Local volume constraints on the L-beam, $c = 418.959$; (b) total porous design of the L-beam. $R_1 \times R_2 = 30 \times 3$, $c = 530.544$.
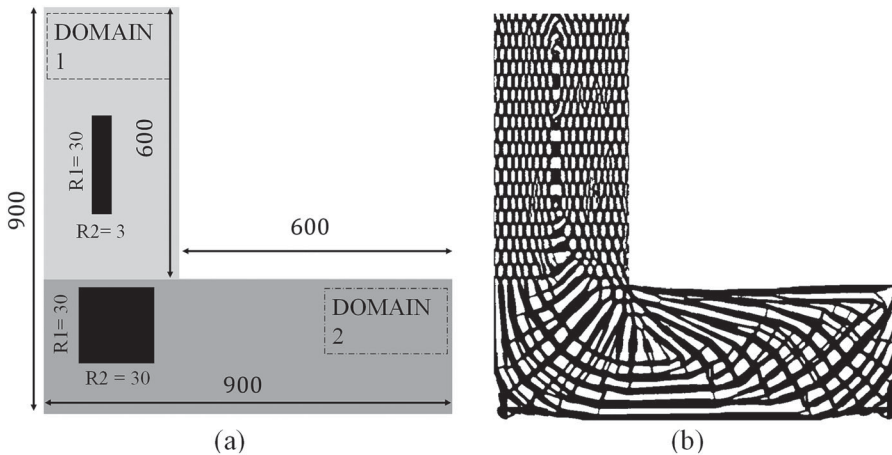
Figure 16. (a) Split design domain; (b) optimized porous L-beam, $c = 518.897$.

of the structure. On the other hand, elongated subdomains will not provide a horizontal part with equivalent stiffness to square subdomains. Therefore, to maximize the robustness of the ensemble, the beam is split into two large domains, domain 1 and domain 2, as described in Figure 16(a). Continuing with the usual procedure, each domain, 1 and 2, is split into smaller subdomains, and a material redistribution process is performed in each of them.

The design domain is discretized with a unique finite element mesh, but domain 1 is split into subdomains of size $R_1 \times R_2 = 30 \times 3$ that prevent the formation of elongated substructures, while domain 2 is split into square subdomains of size $R_1 \times R_2 = 30 \times 30$. This aspect ratio maximizes the freedom of the algorithm to distribute the material. The sensitivity analysis and filtering are performed globally so that the transition from one domain to the other is smooth and continuous. The porous structure resulting from the latter splitting strategy is given in Figure 16(b), and from the value of its compliance, it can be deduced that it is a more rigid structure than the one in Figure 15(b). This exercise demonstrates that the proposed procedure can simultaneously work with subdomains of different size and aspect ratios, resulting in porous structures formed by smoothly connected substructures.

9. Conclusions

This article presents a discrete variable method for infill optimization using the SERA method. It provides an alternative approach for integrating local volume restrictions within the conventional topology optimization formulation to encourage lattice structures that resemble porous structures, an ideal solution for the interior of additively manufactured parts. The results obtained for the analysed benchmark examples agree with the lightweight porous structures generated with other density-based methods. Furthermore, unidirectional growth can be controlled using mixed rectangular subdomains with different aspect ratios to simulate natural bone-like remodelling and generate more sparsely distributed structures. Since the method is based on discrete variables, the obtained solutions are solid/void topologies, and only a basic sensitivity filtering step is involved. The performance of the proposed approach is widely studied in the article by studying different volume fractions, filter radii, and subdomain size and aspect ratios, demonstrating the versatility of the presented technique. Finally, and although not presented in this work, which focused on developing a two-dimensional procedure, the authors and others are currently working on extensions of the proposed strategy to three-dimensional and shell–infill optimization problems.

Disclosure statement

No potential conflict of interest was reported by the authors.

Data availability statement

The original SERA MATLAB® code is openly available in Porous structures_Bilbao School of Engineering Topology Optimization Group at https://data.mendeley.com/datasets/j9jhn2nsjv/1

ORCID

Alain Garaigordobil http://orcid.org/0000-0002-0361-6770
Rubén Ansola http://orcid.org/0000-0001-6405-4006

References

Alonso, Cristina, Rubén Ansola, Estrella Veguería, and Osvaldo M. Querin. 2014. "Results Comparison between SIMP and SERA for Compliant Mechanisms Design." *Book of Abstracts of EngOpt 2014, International Conference on Engineering Optimization.*

Alonso Gordoa, Cristina, Ruben Ansola, Osvaldo Querin, and Vegueria Estrella. 2012. "Parameter Study of a SERA Method to Design Compliant Mechanism." *12th AIAA Aviation Technology, Integration, and Operations (ATIO) Conference and 14th AIAA/ISSMO Multidisciplinary Analysis and Optimization Conference.* Reston, VA: American Institute of Aeronautics and Astronautics. doi:10.2514/6.2012-5525.

Ansola Loyola, Rubén, Osvaldo M. Querin, Alain Garaigordobil Jiménez, and Cristina Alonso Gordoa. 2018. "A Sequential Element Rejection and Admission (SERA) Topology Optimization Code Written in Matlab." *Structural and Multidisciplinary Optimization* 58 (3): 1297–1310. doi:10.1007/s00158-018-1939-x.

Bendsøe, M. P. 1989. "Optimal Shape Design as a Material Distribution Problem." *Structural Optimization* 1 (4): 193–202. doi:10.1007/BF01650949.

Bendsøe, Martin P., and Ole Sigmund. 2004. *Topology Optimization: Theory, Methods and Applications.* Berlin: Springer. doi:10.1007/978-3-662-05086-6.

Bendsøe, Martin Philip, and Noboru Kikuchi. 1988. "Generating Optimal Topologies in Structural Design Using a Homogenization Method." *Computer Methods in Applied Mechanics and Engineering* 71 (2): 197–224. doi:10.1016/0045-7825(88)90086-2.

Brodie, R. N., Osvaldo M. Querin, D. C. Barton, and George I. N. Rozvany. 2004. "Development and Application of the SERA Method for Topology Optimization." *ASMO UK/ISSMO Conference on Engineering Design Optimization*, Stratford-upon-Avon.

Cheng, Lin, Xuan Liang, Eric Belski, Xue Wang, Jennifer M. Sietins, Steve Ludwick, and Albert To. 2018. "Natural Frequency Optimization of Variable-Density Additive Manufactured Lattice Structure: Theory and Experimental Validation." *Journal of Manufacturing Science and Engineering* 140 (10), doi:10.1115/1.4040622.

Clausen, Anders, Niels Aage, and Ole Sigmund. 2015. "Topology Optimization of Coated Structures and Material Interface Problems." *Computer Methods in Applied Mechanics and Engineering* 290 (June): 524–541. doi:10.1016/j.cma.2015.02.011.

Clausen, Anders, Niels Aage, and Ole Sigmund. 2016. "Exploiting Additive Manufacturing Infill in Topology Optimization for Improved Buckling Load." *Engineering* 2 (2): 250–257. doi:10.1016/J.ENG.2016.02.006.

Da, D. C., X. Y. Cui, K. Long, and G. Y. Li. 2017. "Concurrent Topological Design of Composite Structures and the Underlying Multi-phase Materials." *Computers & Structures* 179 (January): 1–14. doi:10.1016/j.compstruc.2016.10.006.

Dapogny, Charles, Rafael Estevez, Alexis Faure, and Georgios Michailidis. 2019. "Shape and Topology Optimization Considering Anisotropic Features Induced by Additive Manufacturing Processes." *Computer Methods in Applied Mechanics and Engineering* 344 (February): 626–665. doi:10.1016/j.cma.2018.09.036.

Deaton, Joshua D., and Ramana V. Grandhi. 2014. "A Survey of Structural and Multidisciplinary Continuum Topology Optimization: Post 2000." *Structural and Multidisciplinary Optimization* 49 (1): 1–38. doi:10.1007/s00158-013-0956-z.

Gao, Wei, Yunbo Zhang, Devarajan Ramanujan, Karthik Ramani, Yong Chen, Christopher B. Williams, Charlie C.L. Wang, Yung C. Shin, Song Zhang, and Pablo D. Zavattieri. 2015. "The Status, Challenges, and Future of Additive Manufacturing in Engineering." *Computer-Aided Design* 69 (December): 65–89. doi:10.1016/j.cad.2015.04.001.

Garaigordobil, Alain, Rubén Ansola, Osvaldo M. Querin, and Igor Fernandez de Bustos. 2020. "Infill Optimization with the Sequential Element Rejection and Admission Method: Porous Structures for Additive Manufacturing." *High Performance and Optimum Design of Structures and Materials IV* 196: 229–239. doi:10.2495/HPSM200231.

Gibson, Ian, David W. Rosen, and Brent Stucker. 2010. "Design for Additive Manufacturing." In *Additive Manufacturing Technologies*, 299–332. Boston, MA: Springer. doi:10.1007/978-1-4419-1120-9_11.

Groen, Jeroen P., Jun Wu, and Ole Sigmund. 2019. "Homogenization-Based Stiffness Optimization and Projection of 2D Coated Structures with Orthotropic Infill." *Computer Methods in Applied Mechanics and Engineering* 349 (June): 722–742. doi:10.1016/j.cma.2019.02.031.

Helou, Mark, and Sami Kara. 2018. "Design, Analysis and Manufacturing of Lattice Structures: An Overview." *International Journal of Computer Integrated Manufacturing* 31 (3): 243–261. doi:10.1080/0951192X.2017.1407456.

Kang, Zhan, and Yiqiang Wang. 2011. "Structural Topology Optimization Based on Non-Local Shepard Interpolation of Density Field." *Computer Methods in Applied Mechanics and Engineering* 200 (49–52): 3515–3525. doi:10.1016/j.cma.2011.09.001.

Long, Kai, Dan Han, and Xianguang Gu. 2017. "Concurrent Topology Optimization of Composite Macrostructure and Microstructure Constructed by Constituent Phases of Distinct Poisson's Ratios for Maximum Frequency." *Computational Materials Science* 129 (March): 194–201. doi:10.1016/j.commatsci.2016.12.013.

Lu, Lin, Baoquan Chen, Andrei Sharf, Haisen Zhao, Yuan Wei, Qingnan Fan, Xuelin Chen, Yann Savoye, Changhe Tu, and Daniel Cohen-Or. 2014. "Build-to-Last: Strength to Weight 3D Printed Objects." *ACM Transactions on Graphics* 33 (4): 1–10. doi:10.1145/2601097.2601168.

Plocher, János, and Ajit Panesar. 2019. "Review on Design and Structural Optimisation in Additive Manufacturing: Towards Next-Generation Lightweight Structures." *Materials and Design*. doi:10.1016/j.matdes.2019.108164.

Querin, O. M., G. P. Steven, and Y. M. Xie. 1998. "Evolutionary Structural Optimisation (ESO) Using a Bidirectional Algorithm." *Engineering Computations* 15 (8): 1031–1048. doi:10.1108/02644409810244129.

Querin, Osvaldo M., Mariano Victoria, Cristina Alonso, Rubén Ansola, and Pascual Martí. 2017. *Topology Design Methods for Structural Optimization*. London: Elsevier.

Rozvany, G. I. N. 2009. "A Critical Review of Established Methods of Structural Topology Optimization." *Structural and Multidisciplinary Optimization* 37 (3): 217–237. doi:10.1007/s00158-007-0217-0.

Rozvany, G. I. N., M. Zhou, and T. Birker. 1992. "Generalized Shape Optimization Without Homogenization." *Structural Optimization* 4 (3–4): 250–252. doi:10.1007/BF01742754.

Rozvany, George, and Osvaldo Querin. 2002. "Theoretical Foundations of Sequential Element Rejections and Admissions (SERA) Methods and Their Computational Implementation in Topology Optimization." *9th AIAA/ISSMO Symposium on Multidisciplinary Analysis and Optimization*. Reston, VA: American Institute of Aeronautics and Astronautics. doi:10.2514/6.2002-5521.

Sigmund, O., and J. Petersson. 1998. "Numerical Instabilities in Topology Optimization: A Survey on Procedures Dealing with Checkerboards, Mesh-Dependencies and Local Minima." *Structural Optimization* 16 (1): 68–75. doi:10.1007/BF01214002.

Sigmund, Ole, and Kurt Maute. 2013. "Topology Optimization Approaches." *Structural and Multidisciplinary Optimization* 48 (6): 1031–1055. doi:10.1007/s00158-013-0978-6.

Wang, Yaguang, and Zhan Kang. 2018. "A Level Set Method for Shape and Topology Optimization of Coated Structures." *Computer Methods in Applied Mechanics and Engineering* 329 (February): 553–574. doi:10.1016/j.cma.2017.09.017.

Wu, Jun, Niels Aage, Rudiger Westermann, and Ole Sigmund. 2018. "Infill Optimization for Additive Manufacturing—Approaching Bone-Like Porous Structures." *IEEE Transactions on Visualization and Computer Graphics* 24 (2): 1127–1140. doi:10.1109/TVCG.2017.2655523.

Wu, Jun, Anders Clausen, and Ole Sigmund. 2017. "Minimum Compliance Topology Optimization of Shell–Infill Composites for Additive Manufacturing." *Computer Methods in Applied Mechanics and Engineering* 326 (November): 358–375. doi:10.1016/j.cma.2017.08.018.

Wu, Jun, Charlie C.L. Wang, Xiaoting Zhang, and Rüdiger Westermann. 2016. "Self-Supporting Rhombic Infill Structures for Additive Manufacturing." *Computer-Aided Design* 80 (November): 32–42. doi:10.1016/j.cad.2016.07.006.

Zhang, Huikai, Yaguang Wang, and Zhan Kang. 2019. "Topology Optimization for Concurrent Design of Layer-Wise Graded Lattice Materials and Structures." *International Journal of Engineering Science* 138 (May): 26–49. doi:10.1016/j.ijengsci.2019.01.006.